Available online at www.sciencedirect.com
ScienceDirect
Journal of Power Sources 169 (2007) 25–34
JOURNAL OF POWER SOURCES
www.elsevier.com/locate/jpowsour

An assessment on convective and radiative heat transfer modelling in tubular solid oxide fuel cells☆

D. Sánchez*, A. Muñoz, T. Sánchez

Escuela Técnica Superior de Ingenieros de Sevilla, Camino de los descubrimientos s/n, 41092 Sevilla, Spain

Available online 6 February 2007

Abstract

Four models of convective and radiative heat transfer inside tubular solid oxide fuel cells are presented in this paper, all of them applicable to multidimensional simulations. The work is aimed at assessing if it is necessary to use a very detailed and complicated model to simulate heat transfer inside this kind of device and, for those cases when simple models can be used, the errors are estimated and compared to those of the more complex models.

For the convective heat transfer, two models are presented. One of them accounts for the variation of film coefficient as a function of local temperature and composition. This model gives a local value for the heat transfer coefficients and establishes the thermal entry length. The second model employs an average value of the transfer coefficient, which is applied to the whole length of the duct being studied. It is concluded that, unless there is a need to calculate local temperatures, a simple model can be used to evaluate the global performance of the cell with satisfactory accuracy.

For the radiation heat transfer, two models are presented again. One of them considers radial radiation exclusively and, thus, radiative exchange between adjacent cells is neglected. On the other hand, the second model accounts for radiation in all directions but increases substantially the complexity of the problem. For this case, it is concluded that deviations between both models are higher than for convection. Actually, using a simple model can lead to a not negligible underestimation of the temperature of the cell.

Keywords: Solid oxide; Fuel cell; Convection; Radiation; Radiosity

1. Introduction

SOFCs are devices operating at temperatures ranging from 800 to 1050 °C for state of the art materials. Below this range, voltage losses due to ionic/electronic resistivity of materials increase noticeably as conductivity grows exponentially with temperature [1,2]. On the other hand, SOFCs cannot be operated continuously at a very high temperature, say 1100 °C, as this would lead to a considerable decrease in performance, probably caused by a thermal expansion mismatch between electrodes and electrolyte [3]. Therefore, the management of heat transfer inside a solid oxide fuel cell, either with tubular or planar technology, is essential in order to guarantee the reliability and long life demanded by the market to this sort of power generation devices. Fig. 1 shows the amount of energy released and/or consumed inside an SOFC fed with natural gas as a function of operating voltage and for different pressures.

Three reactions are considered to take place: hydrogen oxidation, Eq. (1), methane reforming, Eq. (2), and carbon monoxide shifting, Eq. (3).

$$H_2 + \tfrac{1}{2}O_2 \rightarrow H_2O \quad (1)$$

$$CH_4 + H_2O \rightarrow 3H_2 + CO \quad (2)$$

$$CO + H_2O \rightarrow H_2 + CO_2 \quad (3)$$

The net amount of heat released according to Fig. 1 must be evacuated from inside the cell by the air mass flow, which is supplied well in excess with respect to the stoichiometry of Eq. (1). Thus, under normal operating conditions, only 15–20% of the air is used to oxidize the fuel.

This work deals with heat transfer characterization and modelling inside tubular SOFCs, particularly applied to a 1.5 m long Siemens Westinghouse cell with 100 W rated power for ambi-

☆ This paper presented at the 2nd National Congress on Fuel Cells, CONAPPICE 2006.

* Corresponding author. Tel.: +34 954 48 64 88; fax: +34 954 48 72 43.
E-mail address: davidsanchez@esi.us.es (D. Sánchez).

0378-7753/$ – see front matter © 2007 Elsevier B.V. All rights reserved.
doi:10.1016/j.jpowsour.2007.01.076

Nomenclature

A	cross-sectional area [m^2]
ASP	air supply pipe
$\boldsymbol{CT}$	matrix of heat transfer coefficients
D	diameter [m]
f	friction factor
F	view factor
$\boldsymbol{G}$	vector of generation terms
h_{cv}	convective heat transfer coefficient [$W\,m^{-2}\,K^{-1}$]
J	radiosity [$W\,m^{-2}$]
k	thermal conductivity [$W\,m^{-1}\,K^{-1}$]
L	cell length [m]
$\dot{m}$	mass flow [$kg\,s^{-1}$]
n	slice number
Nu	Nusselt number
Pr	Prandtl number
q	heat flow per unit area [$W\,m^{-2}$]
Q	total heat flow [W]
Re	Reynolds number
S	wall surface [m^2]
T	temperature [K]
$\boldsymbol{T}$	vector of temperatures [K]
U_f	fuel utilization factor [%]
x	molar fraction
x_{entry}	thermal entry length [m]

Greek symbols

α	fluid property
ε	emissivity
μ	dynamic viscosity [μP]
σ	Steffan–Boltzmann's constant

Subscripts

an	anode
ca	cathode
h	hydraulic
J	relative to radiosity
lam	laminar
t	iteration step
tur	turbulent
T	relative to temperature
wall	property of a wall/surface

Superscripts

*	normalized view factor

ent pressure operation, Fig. 2. More precise geometric data of this technology can be found in reference [4] and is shown in Table 1.

As said before, heat released in Eq. (1) is evacuated from the electrodes/electrolyte solid structure, also known as PEN from Positive Electrolyte Negative, mainly by convection but, in the case of the tubular technology shown in Fig. 2, radiation between PEN and air supply pipe also plays an important role. Fig. 3 shows the proportion of total heat transfer which takes

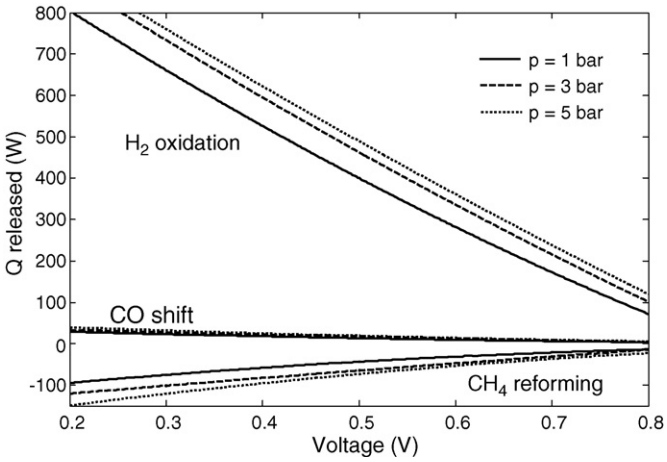

Fig. 1. Heat released (+) and consumed (−) inside the cell.

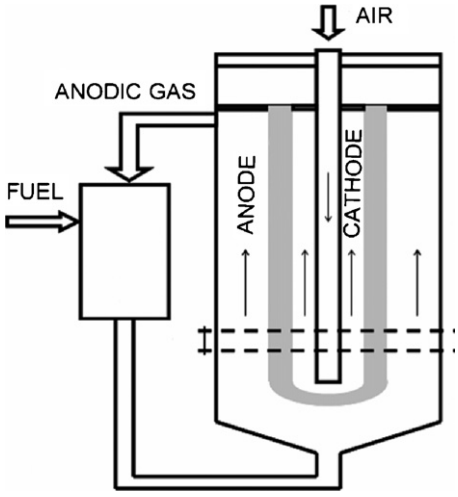

Fig. 2. Reference geometry.

place by convection and radiation. It can be concluded that each one of these heat transfer mechanisms is dominant at a different part of the cell: convection for the first third of it and radiation from that point to the exhaust section. Although this distribution is not constant and may vary according to operating conditions, it is clear that these two phenomena must be very well described when developing a model of performance suitable for tubular SOFCs.

The work is divided in two parts. First, a model for describing convective heat transfer, based on a local evaluation of transfer coefficients, is proposed. This model is later simplified and the loss of accuracy evaluated. Secondly, two models of radia-

Table 1
Reference geometry

Length [m]	1.5
Anode outer diameter [mm]	22
Anode thickness [μm]	100
Electrolyte thickness [μm]	40
Cathode thickness [mm]	2.2
Metallic interconnection thickness [μm]	85

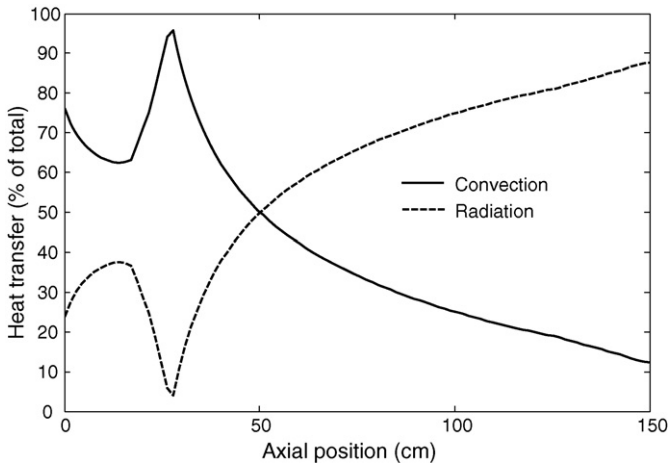

Fig. 3. Heat transfer by convection/radiation.

tive heat transfer are proposed. One of them is a simple model, extensively used in previous works, for radiative exchange in the radial direction which is based on the hypothesis of infinite walls. Then, a complete model of radiation is described. This second model considers radiative exchange in all directions, radially and obliquely, and introduces additional complexity to heat balance equations.

Fig. 4 shows the discretization of the cell which is used for the heat transfer models. The cell is divided axially into a number of slices which are again divided radially into five annular volumes, cylindrical for the inner one, called elements.

It is commonly agreed that multidimensional models of performance of an SOFC are based on a decoupled solving strategy for temperatures and composition. In other words, an iterative method is used that solves thermal and electrochemical models consecutively [5]. Firstly, temperatures are calculated by solving the system of linear equations resulting from local heat balance equations. Compositions and current density remain constant at all the slices and elements. This system of equations is shown in Eq. (4) where $\boldsymbol{T}$ stands for local temperatures, $\boldsymbol{CT}$ for heat transfer coefficients and $\boldsymbol{G}$ for generation terms:

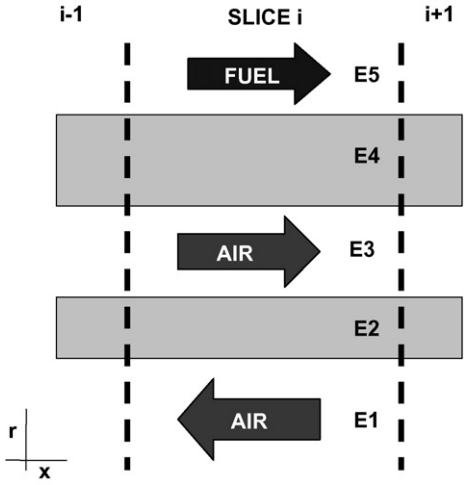

Fig. 4. Elements in a slice.

$$\boldsymbol{CT} \cdot \boldsymbol{T} = \boldsymbol{G} \tag{4}$$

This temperature field is then used as an input to solve the electrochemical model and obtain compositions, current density, voltage losses, reaction rates, etc.

As stated above, this work is aimed at describing radiative and convective heat transfer equations involved in heat balance local equations. In other words, models will be presented to calculate coefficients included in $\boldsymbol{CT}$, Eq. (4).

2. Convective heat transfer: model description

Convective heat transfer is described by Newton's law of cooling:

$$q_{\text{conv}} = h_{\text{cv}}(T_{\text{wall}} - T_{\text{gas}}) \tag{5}$$

where h_{cv} is the convective heat transfer or film coefficient. Calculating this coefficient accurately is the key task to obtaining a precise heat transfer model. The following lines describe a step-by-step procedure to obtain h_{cv}:

1. Calculation of fluid properties: viscosity and thermal conductivity.
2. Calculation of Reynolds number from fluid properties and duct geometry.
3. Calculation of flow regime from Reynolds number.
4. Calculation of Nusselt number and, consequently, convective heat transfer coefficient.

2.1. Properties of gases

Two gas properties are needed to evaluate h_{cv} at each wall: dynamic viscosity and thermal conductivity. However, two major difficulties emerge that make it complex. Firstly, the lack of experimental data at the very high temperature and particular composition which are characteristic of SOFCs, especially for conductivity. Besides, these two properties do not depend on composition proportionally because of the very different behaviours of most of the seven species considered in the mixture: methane, carbon monoxide, carbon dioxide, hydrogen, water vapour, oxygen and nitrogen. In other words, they cannot be calculated with a general expression like:

$$\alpha_{\text{gas}}(T) = \sum_{i=1}^{7} \alpha_i \cdot x_i \tag{6}$$

which is valid for specific heat for example. α_i and x_i stand for property and molar fraction of pure components, respectively, in Eq. (6).

The first step is calculating the dynamic viscosity of pure components as a function of temperature. For this purpose, a fifth order polynomial given in reference [6] is used, Eq. (7).

Table 2
Coefficients for dynamic viscosity and conductivity calculations

	CH_4	CO	CO_2	H_2	H_2O	O_2	N_2
$a_{\mu,1}$	−9.9989	−4.9137	−20.434	15.553	−6.7541	−1.6918	1.2719
$a_{\mu,2}$	529.37	793.65	680.07	299.78	244.93	889.75	771.45
$a_{\mu,3}$	−543.82	875.90	−432.49	−244.34	419.50	−892.79	−809.20
$a_{\mu,4}$	548.11	883.75	244.22	249.41	−522.38	905.98	832.47
$a_{\mu,5}$	−367.06	−572.14	−85.929	−167.51	348.12	−598.36	−553.93
$a_{\mu,6}$	140.48	208.42	14.450	62.966	−126.96	221.64	206.15
$a_{\mu,7}$	−22.920	−32.298	−0.4564	−9.9892	19.591	−34.754	−32.430
$a_{k,1}$	0.4796	−0.2815	2.8888	1.5030	2.0103	−0.1857	−0.3216
$a_{k,2}$	1.8732	13.999	−27.018	62.892	−7.9139	11.118	14.810
$a_{k,3}$	37.413	−23.186	129.65	−47.190	35.922	−7.3734	−25.473
$a_{k,4}$	−47.440	36.018	−233.29	47.763	−41.390	6.7130	38.837
$a_{k,5}$	38.251	−30.818	216.83	−31.939	35.993	−4.1797	−32.133
$a_{k,6}$	−17.283	13.379	−101.12	11.972	−18.974	1.4190	13.493
$a_{k,7}$	3.2774	−2.3224	18.698	−1.8954	4.1531	−0.2278	−2.2741

Coefficients $a_{i,n}$ can be found in Table 2.

$$\mu\,(\mu\mathrm{P}) = \sum_{n=1}^{6} a_{\mu,n}\left(\frac{T\,(\mathrm{K})}{1000}\right)^{n} \tag{7}$$

A similar expression is used for thermal conductivity:

$$k\,(\mathrm{W\,m^{-1}\,K^{-1}}) = 0.01\sum_{n=1}^{6} a_{k,n}\left(\frac{T\,(\mathrm{K})}{1000}\right)^{n} \tag{8}$$

Next step after calculating pure components properties is to evaluate those of the mixture. According to the work by Todd and Young [6], where several methods used to calculate fluid properties are studied and compared, the most accurate methods are Reichenberg's and Wassiljevas's for viscosity and conductivity, respectively. Expressions for these methods are rather complex and will not be quoted here; however, readers wishing to know full expressions are referred to [6].

2.2. Reynolds number

Reynolds number evaluates the ratio of viscosity to inertia of a gas or liquid stream and is representative of the flow regime of a stream. The following general expression of *Re* inside a duct is used:

$$Re = \frac{\dot{m}\,D_\mathrm{h}}{\mu A} \tag{9}$$

where A is the cross-sectional area, $\dot{m}$ the mass flow and D_h is the hydraulic diameter or characteristic length of the duct. This diameter is different for each duct:

1. Air supply pipe. Hydraulic and geometric diameters are the same.

$$D_\mathrm{h} = D_\mathrm{ASP,in} \tag{10}$$

2. Annular duct. The hydraulic diameter is:

$$D_\mathrm{h} = D_\mathrm{ca,in} - D_\mathrm{ASP,out} \tag{11}$$

3. Anodic duct. As shown in Fig. 5, the geometry of the anodic duct is rather complex and its hydraulic diameter is calculated from Eq. (12):

$$D_\mathrm{h} = 4\frac{\text{Cross-sectional area}}{\text{Wet perimeter}} = \frac{4-\pi}{\pi} D_\mathrm{an,out}. \tag{12}$$

2.3. Flow regime and entry length

Three cases are considered when studying the flow regime of each stream according to *Re*:

1. Laminar flow, thermal entry length.
2. Laminar flow, fully developed.
3. Turbulent flow, fully developed.

Although many authors claim that fully turbulent flow is not guaranteed below 10,000, a critical value of *Re* is set at 2300 according to [1,7,8]. For laminar flow, the following thermal entry length is considered [7]

$$x_\mathrm{entry,lam} = 0.0575\,Re\,Pr\,D_\mathrm{h} \tag{13}$$

where thermal and hydrodynamic boundary layers develop simultaneously due to a Prandtl number close to unity, $Pr = 0.7$. For turbulent flow, the evaluation of entry length is more com-

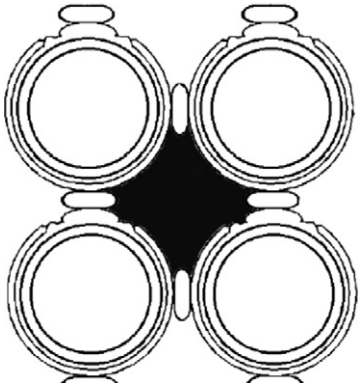

Fig. 5. Cross-sectional view of anodic duct.

Table 3
Nusselt number

$x^* = x/Re \cdot Pr \cdot D$	Nu_x
0.001	16.8
0.002	12.6
0.004	9.6
0.006	8.25
0.010	6.8
0.020	5.3
0.050	4.2
∞	3657

Laminar entry length.

plex as the transition from undeveloped to fully developed flow is thought to take place somewhere inside the range:

$$10 \leq \frac{x_{\text{entry,turb}}}{D_h} \leq 60. \quad (14)$$

The ratio of total length to hydraulic diameter of the ducts involved in this study ranges from 150, air supply pipe, to 280, annular duct. For these geometric "boundary" conditions, the turbulent entry length is considered negligible.

2.4. Nusselt number: convective heat transfer coefficient

The heat transfer model presented in this work is the evolution of a multidimensional SOFC model previously developed by the authors [5,9] which predicts temperatures and compositions locally, at each point of the cell. Thus, the evaluation of heat transfer coefficients, i.e. *Nu*, must include a dependence on position, and consequently composition, inside the cell.

Nusselt number is calculated from correlations fitted to empirical data, either by means of mathematical expressions or tables. Most of these expressions give values for average *Nu* along the whole duct and only a few of them are applicable to local studies. The latter will be used in this work.

Values of *Nu* in Table 3 [8] are used for the laminar entry length. Interpolation is used between given non-dimensional positions x^*. The last value of *Nu* in Table 3 corresponds to the value for fully developed laminar flow which holds constant at 3.657 for any value of *Re* or *x*.

For $Re > Re_c$, flow is turbulent and Gnielinski's equation is used to evaluate *Nu*, Eqs. (15) and (16) [7], where *f* stands for friction factor in Eq. (16).

$$Nu = \frac{(f/8)(Re - 1000)Pr}{1 + 12.7\sqrt{(f/8)}(Pr^{2/3} - 1)} \left(1 + \left(\frac{D_h}{L}\right)^{2/3}\right) \quad (15)$$

$$f = \frac{1}{0.79\ln(Re) - 1.64} \quad (16)$$

Gienelinski's equation is applicable to $Re > 2300$, $0.5 < Pr < 2000$ and $L > D_h$. The complexity of Eqs. (15) and (16) leads some authors to employ simpler equations like Colburn's, shown in Eq. (17), which is valid for $Re > 10{,}000$, $0.7 < Pr < 160$ and $L > 10D_h$. This correlation is easier to evaluate but can lead to errors as high as 20% as shown in Fig. 6 [10]. In addition, the uncertainty in the range of *Re* from 2300, end of laminar, to 10,000, Eq. (17) validity, is significantly higher than when using Gnielinski's correlation.

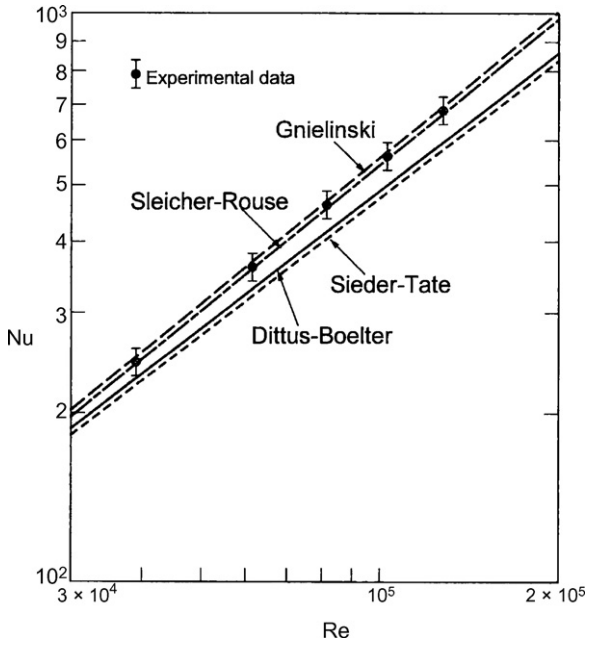

Fig. 6. Correlations for turbulent flow [10].

$$Nu = 0.023\, Re^{4/5} Pr^{1/3} \quad (17)$$

Finally, the convective heat transfer coefficient is evaluated directly from the value of *Nu* through the following equation:

$$h_{cv} = \frac{Nu\, k}{D_h} \quad (18)$$

The method described above is based on substituting D_h by *x*, axial position, in Eq. (15) and gives a value of *Nu* which is not the real value of local *Nu*. Fig. 7 shows that there is an underestimation with respect to the actual local *Nu*. However, the error made when using this approach is small and does not increase substantially the uncertainty in the value of heat transfer coefficients.

3. Radiative heat transfer: model description

Previous works by the authors have shown that radiation involves not only heat exchanged between solid walls but

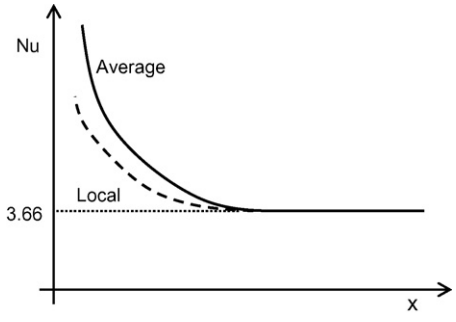

Fig. 7. Comparison between local and average Nusselt for internal forced flow.

between a solid wall and certain gases. However, the latter is out of the scope of this work as it is only relevant under abnormal operation inside the cell, i.e. high current density [5,9].

Two models are to be presented in the following lines. One of them is a so-called radial model and is based on the hypothesis of infinite coaxial cylinders. It will be called the simple model. A more complex model will be presented later, which accounts for oblique radiation between axially adjacent cells. This model, called complex model, makes it necessary to introduce a new unknown for each wall involved in the radiative exchange.

In both models, exchanging walls are considered to be grey walls satisfying Kirchhoff's laws.

3.1. Simple model: infinite parallel exchanging walls

This simple model assumes exchanging walls to be infinitely long and, thus, only radiation between walls of the same slice, Fig. 4, is considered. In addition, this hypothesis reduces the radiative exchange to the walls of the annular cathodic duct as long as wall temperatures are considered to be constant at each slice. In other words, for the inner duct of the air supply pipe and the anodic duct, the net amount of heat exchanged by radiation between walls is zero.

Eq. (19) defines the net amount of heat exchanged by radiation between the outer wall of the supply pipe ASP and the inner wall of the cathode.

$$Q_{\text{rad}} = \frac{\sigma \cdot (T_{\text{cathode}}^4 - T_{\text{ASP}}^4)}{(1/\varepsilon_{\text{cathode}}) + (D_{\text{cathode}}/D_{\text{ASP}})((1/\varepsilon_{\text{ASP}}) - 1)} \times \pi \cdot D_{\text{cathode}} \cdot \Delta x \tag{19}$$

The view factor between inner and outer surfaces of the duct is 1 for $F_{\text{ASP,cat}}$ and the ratio of diameters for $F_{\text{cat,ASP}}$.

The radiative flow calculated from Eq. (19) forms part of the linear system of equations used to solve the thermal model of the fuel cell, Eq. (4), where $\boldsymbol{T}$ is a vector containing temperatures to be calculated, five for each slice of the cell. $\boldsymbol{CT}$ is a matrix containing temperature coefficients for each heat balance equation and $\boldsymbol{G}$ stores known heat fluxes like heats of reaction. This system of equations has $5N$ unknowns, N being the number of slices that the cell is divided into.

Finally, Eq. (19) must be linearized before added to Eq. (4). To do so, the following approach is used:

$$T_t^4 = 4 \cdot T_{\text{m},t-1}^3 \cdot T_t = 4 \cdot \left(\frac{T_{\text{cat},t-1} + T_{\text{ASP},t-1}}{2} \right)^3 \cdot T_t \tag{20}$$

where $t-1$ and t are the previous and current steps of the iterative process and T_{m} is the arithmetic mean temperature of cathode and air supply pipe. This approach is accurate enough for temperature differences between walls below 50 °C [11].

3.2. Complex model: oblique radiation

The previous model does not consider oblique radiation between adjacent slices so the radiative flow leaving the surface through both annular ends of each slice is dismissed. As discussed later, this is only acceptable for a low number of slices, i.e. high slice length. When this is not the case, the amount of radiation not considered for heat transfer balance equations can be not negligible and lead to high deviation in wall temperature. In such a situation, a more complex description of radiative exchange is needed.

Unfortunately, the complexity of the model which includes oblique radiation is significantly higher than that of the simple model. The radiative exchange inside a multiple wall enclosure cannot be evaluated from temperatures exclusively, and a new set of parameters is needed. In fact, each wall of the domain is characterized not only by its temperature but by its radiosity as well, the latter being the amount of thermal radiation leaving the wall.

At a certain enclosure, the heat flow leaving a surface is determined by the following equation:

$$Q_{\text{rad},i} = \left(J_i - \sum_{\forall j} F_{ij} J_j \right) S_i \tag{21}$$

where J_i is the radiosity of surface i, F_{ij} the view factor between walls i and j, respectively, and S_i is the area of wall i. In order to evaluate radiosities, an equation for each surface is needed, Eq. (22), which links temperature and radiosity at each wall of the enclosure:

$$J_i = \varepsilon_i \sigma T_i^4 + \sum_{\forall j} (1 - \varepsilon_j) F_{ij} J_j \tag{22}$$

where ε_i is the surface emissivity and σ is the Stefan–Boltzman constant. Again, and in order to linearize the system of equations to be solved, the power of temperature to the fourth is expressed in the following manner:

$$T_i^4 = T_{i,t-1}^3 T_{i,t} \tag{23}$$

where i and t stand for surface and iteration step, respectively.

Eqs. (21) and (22) are introduced in the system of equations described in Eq. (4) to form a new one:

$$\begin{bmatrix} \boldsymbol{CT}_{\text{T}} & \boldsymbol{CT}_{\text{J}} \\ \boldsymbol{CJ}_{\text{T}} & \boldsymbol{CJ}_{\text{J}} \end{bmatrix} \begin{bmatrix} \boldsymbol{T} \\ \boldsymbol{J} \end{bmatrix} = \begin{bmatrix} \boldsymbol{G}_{\text{T}} \\ \boldsymbol{G}_{\text{J}} \end{bmatrix} \tag{24}$$

$\boldsymbol{CT}_{\text{T}}$ stores the coefficients related to temperatures for the heat balance equations at each domain of each slice. $\boldsymbol{CT}_{\text{J}}$ stores the coefficients related to radiosity for the same heat balance equations; in this case, the coefficients are included in the calculation of radiative heat flows according to Eq. (21). $\boldsymbol{CJ}_{\text{T}}$ and $\boldsymbol{CJ}_{\text{J}}$ store the coefficients related to temperature and radiosity, respectively, in Eq. (22), radiosity balance at each wall. Independent terms $\boldsymbol{G}_{\text{T}}$ and $\boldsymbol{G}_{\text{J}}$ have been reorganized conveniently.

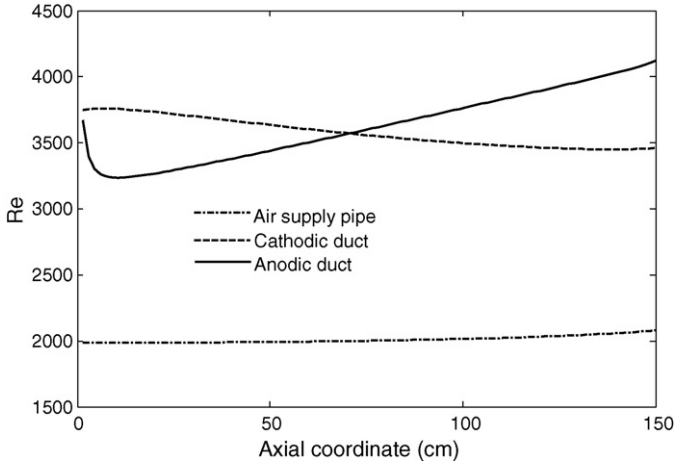

Fig. 8. Local *Re* inside ducts for $V = 0.45$ V.

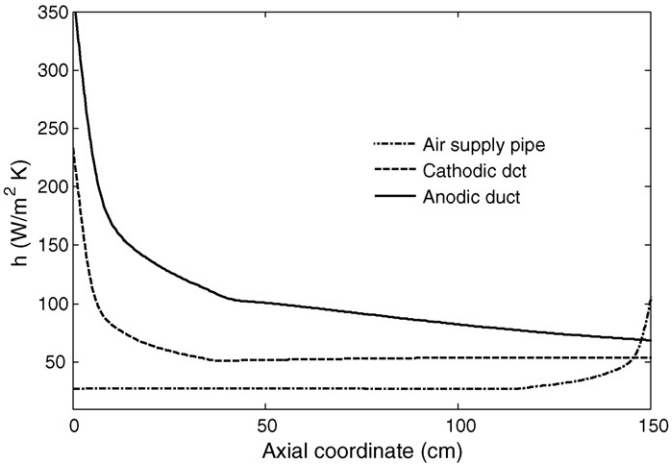

Fig. 10. Computed heat transfer coefficients for $V = 0.62$ V.

4. Convective heat transfer: model results

As said in the introductory section of this work, convective heat transfer coefficients cannot be taken as constant along the cell tube. In fact, as shown in Fig. 8, *Re* varies significantly from the entrance to the exhaust section of any of the three ducts inside the stack, especially at the anode as a consequence of the rapid increase in temperature and mass flow. Convective heat transfer coefficients are depicted in Fig. 9. It can be seen that, for the operating conditions considered, 0.45 V at 80% fuel utilization, laminar flow is only found at the air supply pipe. In this case, it is also easy to identify the thermal entry length, where convective transfer coefficients decrease. Turbulent flow is found at the other two ducts. In addition, at the anodic duct, it must be noticed that *h* varies significantly due to two main causes: first, a strong temperature variation along the first twenty centimetres of the tube; second, an increasing mass flow from the entrance to the exhaust.

However, the values of *h* found at Fig. 9 are not usual for normal operating fuel cells, as practical voltages are around 0.62 V. For these conditions, flow is laminar at all three ducts, which show thermal entry lengths. Heat transfer coefficients for this case, shown in Fig. 10, are closer to reality.

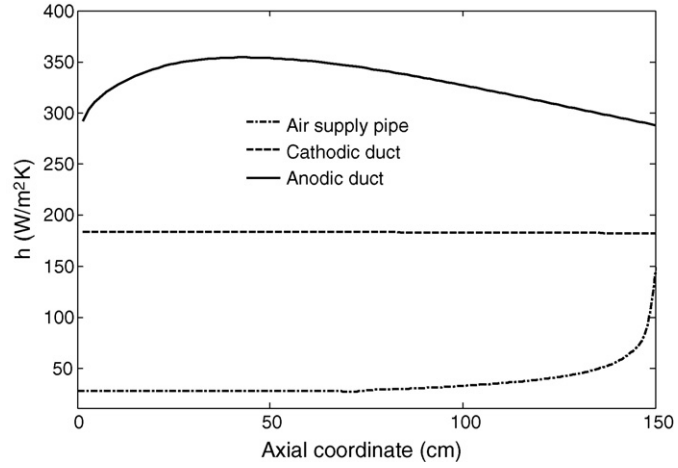

Fig. 9. Computed heat transfer coefficients for $V = 0.45$ V.

At this point, a comparison between both assumptions, constant or variable heat transfer coefficients, is mandatory in order to assess its impact on fuel cell modelling. First, the model has been run for 0.65 and 0.35 V, 80% fuel utilization, 900 °C operating temperature and 3 bar pressure, keeping intake fuel and air flows equal for both cases. Results are shown in Table 4. The first conclusion drawn is that, from a performance point of view, there is no need to consider variations of transfer coefficients inside the cell as its influence on power, current density and other relevant parameters of the cell is hardly one percent of their total value. Only mean temperatures are affected at low current density due to the effect of thermal entry lengths being considered in the detailed model. This effect has been further studied by running the simplified model with a different set of initial and boundary conditions, rightmost column in Table 4. In this case, the air flow entering the cell has been reduced in order to keep the mean temperature around 900 °C, which is the temperature predicted by the detailed model, and 80% fuel utilization. Thus, if the mean temperature were to be kept constant, a little increase in air utilization from 9 to 10% for the base case would arise. However, this difference tends to decrease with increasing current densities as flow becomes turbulent in every duct.

An internal study has also been carried on and, for the cases shown in Table 4, a comparison between internal temperature fields has been done. Results at 0.65 V operating voltage are shown in Fig. 11 for all three cases mentioned above. It can be seen that predicted temperatures are significantly different at both ends of the cell and that the general shape of the curves are similar elsewhere. This behaviour was expected and is caused by the miscalculation of heat transfer coefficients at the thermal entry lengths.

Fig. 11 shows that a difference of around 30 °C exists between all three models at different parts of the cell and, however, according to results in Table 4, this is not noticeable when analyzing the global performance of the stack. It has been said previously that local temperature affects the electrochemical performance of the cell and, thus, it has a major impact on current density. This effect is depicted in Fig. 12, where it can be seen

Table 4
Comparison at constant fuel and air intake flows

	Variable *Nu*		Constant *Nu*		
	0.65 V	0.35 V	0.65 V	0.35 V	0.65 V
Current density [A m^{-2}]	1745	5382	1740	5392	1758
Power [W]	94.6	157.4	94.3	157.4	95.3
Fuel utilization [%]	79.8	80.3	79.5	80.5	79.7
Temperature [°C]	902 (922)	898 (928)	886 (906)	900 (928)	902 (926)

Maximum temperature shown in parentheses in the mean temperature box.

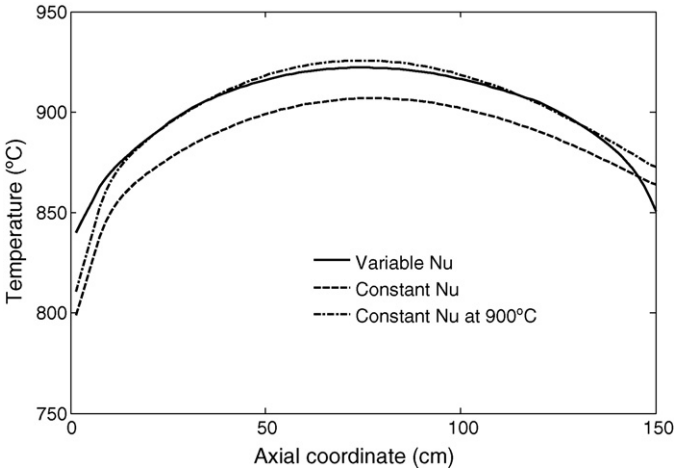

Fig. 11. Solid temperatures.

that the local current density depends strongly on temperature but, as long as the mean temperature is similar for all three cases, the mean current density is equally similar. For this reason, the global performance of the cell is not affected.

5. Radiative heat transfer: model results

Results obtained when applying the simple model have been published in previous works by the authors [9] and other researchers [4] and will not be repeated here. However, it must be said that they have been considered satisfactory as the impact

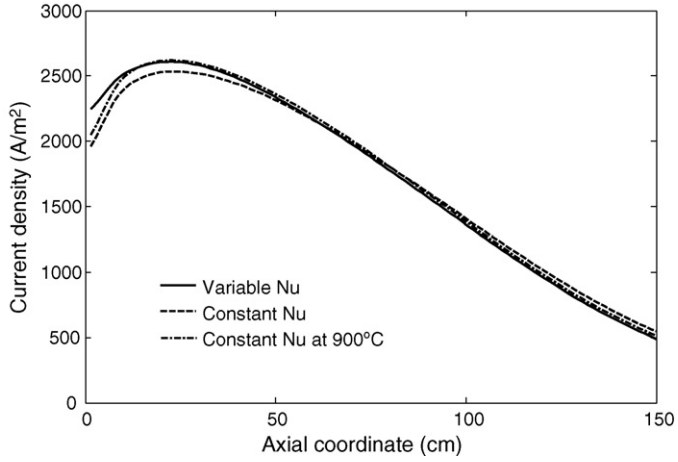

Fig. 12. Current density distribution along the cell.

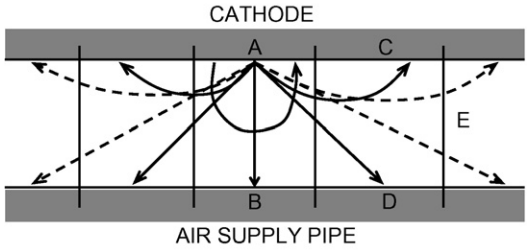

Fig. 13. Radiative exchange of cathode inner face (wall A).

over global performance of using the simple or complex models is not dramatic. This will be shown later.

Fig. 13 shows the complexity of the radiative heat transfer when applying the complex model. A is the inner wall of the cathode of slice n and is exchanging heat by radiation with itself, the inner wall of the cathode of adjacent slices $n+1$ and $n-1$ (wall C) and the outer wall of the air supply pipe of the same slice (wall B) and adjacent slices $n+1$ and $n-1$ (wall D). Radiative exchange with slices further than $n+2$ or $n-2$, depicted in Fig. 13 with dashed lines, is considered to take place as a whole through wall E.

Table 5 shows the calculated view factors when considering 100 slices. For this case, if the radiation exchanged between A and walls further than $n+2$ is not considered, about 20% of the total amount of radiation emitted by A is neglected in the heat balance. In addition, this percentage of radiation lost tends to increase when the number of slices is high and slices get narrower. Two strategies are proposed in order to take this issue into account.

The first method is based on additional exchange equations. Radiation between slices which are further than $n+2$ or $n-2$ can be added until the equivalent F_{AE} view factor is smaller than a maximum value previously established. This method increases the computation time and, as a main drawback, it can generate a badly conditioned exchange matrix $\boldsymbol{CT}_J$ or $\boldsymbol{CJ}_J$ where some elements are too small compared with elements on the main diagonal.

The second approach to the problem is based on neglecting the radiation lost through the virtual wall E and normalizing the

Table 5
View factors for a hundred slices

F_{AB}	F_{AA}	F_{AC}	F_{AD}	F_{AE}
0.4163	0.2095	0.0456	0.0319	0.1096

Table 6
Comparison at constant fuel and air intake flows

	Simple model		Complex model	
	0.65 V	0.35 V	0.65 V	0.35 V
Current density [A m^{-2}]	1721	5259	1745	5382
Power [W]	93.3	153.5	94.6	157.4
Fuel utilization [%]	78.7	78	79.8	80.3
Temperature [°C]	851 (884)	881 (927)	902 (922)	898 (928)

Maximum temperature shown in parentheses in the mean temperature box.

Table 7
Comparison at 80% fuel utilization and 900 °C

	Simple model		Complex model	
	0.65 V	0.35 V	0.65 V	0.35 V
Current density [A m^{-2}]	1721	5259	1745	5382
Power [W]	93.3	153.5	94.6	157.4
Fuel utilization [%]	78.7	78	79.8	80.3
Air utilization [%]	14	7.5	9	6.5
Temperature [°C]	900 (943)	902 (954)	902 (922)	898 (928)

Maximum temperature shown in parentheses in the mean temperature box.

rest of view factors to satisfy the first Kirchhoff's law, Eq. (25):

$$\sum F_{ij} = 1 \tag{25}$$

The view factors are easily normalized to the sum of those considered in order to satisfy Eq. (25). Eq. (26) shows the normalized F_{AB} for the previous case of Fig. 13.

$$F^*_{AB} = \frac{F_{AB}}{F_{AB} + F_{AA} + 2F_{AD} + 2F_{AC}} \tag{26}$$

When applying this second method, care must be taken to evaluate how much radiation is being dismissed as the errors made can be not negligible. However, any of these two approaches proposed is not usually applied separately and the most convenient method to improve accuracy without losing robustness in the solution process is to apply both of them in the order exposed here. Results shown below have been obtained this way.

A comparison between the two models, simple and complex, described previously has been made in order to assess their impact on predicted temperatures. Bearing in mind that the so called complex model doubles the number of equations and unknowns needed to be solved, it is important to know if it is worth increasing the complexity of the model, from the point of view of improving the accuracy of results.

The analysis has been done in two steps, noting that every run of the model has been done on the assumption of variable convective heat transfer coefficients. Firstly, both models have been applied to the same boundary conditions, i.e. air and fuel flows; results are shown in Table 6 in a similar way to Table 4. Differences between both cases are more important than for the convective analysis and range from 1.4% for the power produced to 5.5% for predicted mean and maximum temperatures. Not only this, the fact that temperatures calculated with the simple model are lower than those from the more complex model makes it, although faster, more unsafe to use the former from the point of view of mechanical integrity.

The second step of the analysis has been done assuming that voltage and mean operating temperatures must be kept at the desired 0.65 or 0.35 V and 900 °C, respectively. For the latter, the air flow entering the cell must be reduced when the simple model is applied. Results are shown in Table 7, where air utilization is now added in order to evaluate the reduced air flow needed to keep the operating temperature at the same level when the simple model is used. It can be seen that the difference is not negligible for low current densities where fuel cells usually operate.

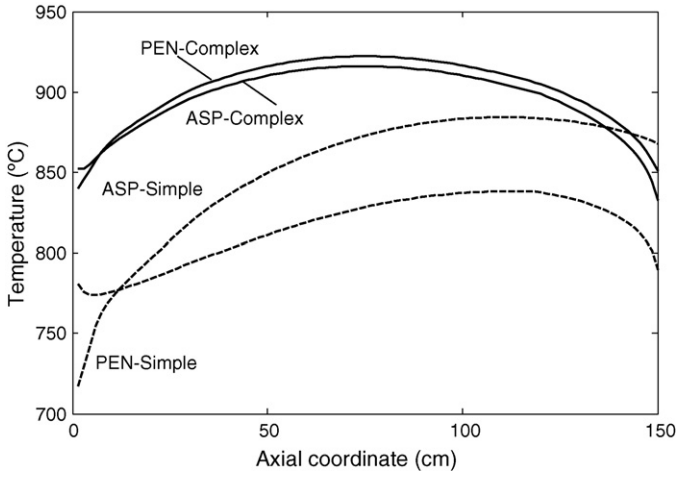

Fig. 14. Predicted temperatures with simple and complex radiation model. ASP: air supply pipe; PEN: positive-electrolyte–negative; 0.65 V, 80% U_f.

According to results shown in Tables 6 and 7, if global performance of the fuel cell is to be evaluated, there is no need to use the complex method to describe radiative heat transfer. The infinite parallel walls assumption works well and errors are kept below 5%. However, evaluating local temperatures can be very important for some researchers devoted to improve the internal performance of the cell. In this case, the simple model cannot be further used. Fig. 14 depicts the difference in predicted internal temperatures when using both methods with the same boundary and initial conditions. Two aspects must be emphasized. Predicted temperatures are higher, giving way to a better performance in terms of power produced, and more stable, i.e. they do not vary very much from the entrance to the exhaust, when the complex model is used. This fact is close to the assumption by Haynes [12], who claim that the solid structure of the cell be at constant temperature along the tube.

6. Conclusions

The work presented here is based on another work previously published by the authors [5]. It focuses on heat transfer modelling inside tubular fuel cells and tries to improve the weakest aspects of those models being used by other authors currently [2,12,13]. The following particular conclusions with respect to the models presented can be drawn:

1. If the model is intended to predict the global performance of the fuel cell and no internal information is needed, complex models are not necessary. In other words, a constant convective heat transfer coefficient with a simple radiation model can be used.
2. The consideration of constant or variable convective heat transfer coefficients has a major impact on temperature at both ends of the cell tube but does not affect the shape of the temperature curve elsewhere.
3. Despite conclusion 1, if internal temperatures need to be evaluated, the simple radiation model is not acceptable as it underestimates temperatures by around 40 °C at usual operating voltages.

Finally, some remarks must be done about the results shown before. Fig. 6 shows the accuracy of correlations to evaluate *Nu* with respect to experimental data. For the most accurate of them, Gnielinski or Schleiser-Rouse, there is still a 10% uncertainty in the calculated value which cannot be avoided. Thus, when the effect of using constant or variable *Nu* is discussed in Section 4, it must be taken into account that deviations of one method with respect to another are added to that uncertainty of, at least 10%. In fact, bearing in mind that *Re* is closer to its critical value, the uncertainty about whether the flow is laminar or turbulent must also be considered.

There is still another effect that might be thought to affect the calculation of convective heat transfer coefficient, the porosity of the wall. This effect is already considered when the mass and heat balance equations are applied to each volume of a slice. Thus, the amount of energy leaving the volume with the gas which is diffusing through the porous walls is included in the calculations.

These two issues addressed here do not affect significantly to the discussions presented in previous sections of the work. Comparisons between results from different models just add deviations from a standard uncertainty which is out of the scope of this work and is, actually, very difficult to eliminate.

References

[1] U.G. Bossel, Final Report on SOFC Data Facts and Figures, Swiss Federal Office of Energy, Berne, 1992.
[2] A. Selimovic, Modelling of Solid Oxide Fuel Cells Applied to the Analysis of Integrated Systems with Gas Turbine, Doctoral Thesis, University of Lund, Lund, 2002.
[3] A. Selimovic, M. Kemm, T. Torrison, M. Assadi, J. Power Sources 145 (2005) 463–469.
[4] S. Campanari, P. Iora, J. Power Sources 132 (2004) 113–126.
[5] D. Sánchez, Aportación al análisis de pilas de combustible de óxido sólido (SOFC) para integración en sistemas híbridos pila de combustible-turbina de gas (in Spanish), Tesis Doctoral, Universidad de Sevilla, Sevilla, 2005.
[6] B. Todd, J.B. Young, J. Power Sources 110 (2002) 186–200.
[7] H.D. Baehr, K. Stephan, Heat and Mass Transfer, Springer, Berlin, 1998.
[8] W.M. Rohsenhow, J. Hartnett, E. Ganic, Handbook of Heat Transfer Fundamentals, second ed., McGraw-Hill, New York, 1973.
[9] D. Sánchez, R. Chacartegui, A. Muñoz, T. Sánchez, J. Power Sources 160 (2006) 1074–1087.
[10] F. Kreith, M.S. Bohn, Principles of Heat Transfer, fourth ed., Harper and Rove, New York, 1986.
[11] F.P. Incropera, D.P. DeWitt, Fundamentals of Heat and Mass Transfer, John Wiley and Sons, New York, 1996.
[12] C. Haynes, Simulation of Tubular Solid Oxide Fuel Cell Behavior for Integration into Gas Turbine Cycles, PhD Thesis, Georgia Institute of Technology, Atlanta, 1999.
[13] C. Stiller, B. Thorud, S. Seljebo, O. Mathisen, H. Karoliussen, O. Bolland, J. Power Sources 141 (2005) 227–240.